Chapter 6

Robust magnetic proximity effect induced adaptive Half-metallicity in Weyl semimetal-ferromagnet van der Waals heterostructure

6.1 Introduction

Two-dimensional (2D) van der Waals (vdW) atomic crystals provide new avenues for engineering active interfaces, making it suitable for the development of low-power nanoscale devices [1-4]. Designing vdW heterostructure by considering MPE manifests constructive strategy to modulate the properties and performance of the system [5-7]. The MPE suggests modified functionality of vdW heterostructure with interfacial coupling of electronic wavefunctions over the interface [8-10]. Recently, proximity effect has been established in graphene-$CrBr_3$ [11, 12], WSe_2-CrI_3 [6, 13], WSe_2-$Cr_2Ge_2Te_6$ [45], WTe_2-Fe_3GeTe_2 [14] and g-C_3N_4/CuSe [15] vdW heterostructures. In general, the spin-polarization can be introduced in non-magnetic system by conventional methods [16], which have limitation in charge and spin-related properties. In this regard, MPE has the possibility to transform the existing nature of a pristine system to a completely new behaviour by modulating spin at interface of vdW atomic crystals and overcomes the aforementioned limitation [17]. Moreover, MPE has high degree of tunability with external stimulus such as strain [18], pressure [19], electric field [20, 44, 46], twisting [21], making it suitable for developing nanoscale devices. MPE can effectively tune the electronic structure and enables to realize topologically non-trivial phases and spin-dependent properties [22-26, 37].

1T' phase of transition metal dichalcogenides (TMDC) material offers promising platform for realizing topologically non-trivial phases and protected spin textures denoted as MX_2 (M: Mo, W; X: S, Se, Te) [27]. Among these, 1T' phase of WTe_2 is the most stable configuration and experimentally favoured. It is also known as Weyl semimetal (WSM) with negative quantum spin Hall (QSH) type insulator [28]. WSM exhibits unusual spin texture, which describes the occurrence of spin polarization in Fermi pockets of bulk bands and surface states [29, 30]. Moreover, WSM are subtly flexible with inclusion of external electric field and introduces spin polarization extrinsically for efficient generation of spin currents [31]. However, a fundamental challenge lies in controlling spin-polarization intrinsically in QSH insulators at room temperature, because of intervention from non-trivial bulk bands [32] and also for nonmagnetic nature. As a consequence, it prohibits elastic backscattering of electrons basically, limiting the design in developing efficient spin switches. In the aspect of controlling spin-polarization inherently, 2D ferromagnet can effortlessly inject spin into WSM and possibly regulate spin polarization by magnetic proximity interaction. As a result, 2D vdW ferromagnet ($CrBr_3$) predominantly highlights the modulation of magnetic ordering at interface in presence of external stimulus [33]. This offers a promising platform by coupling WSM with 2D ferromagnet constructing magnetic vdW heterostructure exclusively via proximity effect and eloquent tuning of electronic structure by external electric field

In this chapter, we consider WSM 1T'-WTe_2 and a 2D ferromagnet, $CrBr_3$ [33] for investigating interfacial phenomena via MPE in the heterostructure system with a lattice strain of 2.9%. Such combination of magnetic vdW heterostructure has the tendency to acquire lattice anisotropy and has the possibility to tune the magnetic behaviour with application of external electric field. Our finding suggests that the spin splitting and 100% spin polarization arise in electronic properties of the heterostructure system via MPE with an interplanar distance

3.68 Å. It is observed that the electronic structure transforms from semiconducting to half-metallic behaviour suggesting the strong presence of MPE. MPE is highly tunable and modulates the energy gap from half metallic to semiconducting as well as overlapping in the presence of external stimulus. The notable enhancement in the magnetic moment value of 4% in heterostructure system is noticed. The presence of built-in electric field due to charge transfer activates the interfacial polarization in the heterostructure system. With an application of external electric field, we find that the magnetic moment value modulates by ±0.04 μ_B/cell due to charge transfer and orbital hybridization at the interface. The combined effect of MPE and electric field in band topology and electronic conductivity reveals the heterostructure system to be promising candidate for fabricating next-generation nanoelectronic devices.

6.2 Model and Computational Details

Magnetic proximity induced spin related phenomena in 1T'-WTe_2/$CrBr_3$ vdW heterostructure is performed under the framework of *ab initio* density functional theory (DFT), as included in Quantum ESPRESSO package [34]. The Perdew-Burke-Ernzerhof (PBE) exchange-correlation functional is taken into account with generalized gradient approximation (GGA) to determine the exchange-correlation coupling [35]. The kinetic energy cut-off is set to 100 Ry for plane wave basis set and the K-point sampling of 1T'-WTe_2/$CrBr_3$ vdW heterostructure is employed with 9 x 9 x 1 unshifted Monkhorst-Pack (MP) grid. We consider weak van der Waals (vdW) forces between 1T'-WTe_2 and $CrBr_3$ isolated layers and the dispersion corrections have been employed by DFT-D method established by Grimme [36], with vdW radius of 3.305 Å, 2.952 Å, 3.575 Å and 3.349 Å for bromine (Br), chromium (Cr), tellurium (Te) and tungsten (W), respectively. Davidson diagonalization scheme is considered over the whole calculation with a convergence criterion of 10^{-10} Ry. The Hellmann-Feynman force convergence is minimized to 10^{-4} Ry/Bohr to obtain the relaxed structure and making it feasible for DFT calculations. The interplanar distance

between 1T'-WTe_2 and $CrBr_3$ layer is kept constant with 3.68 Å with a lattice strain of 2.9%. The vacuum region is set to be about 30 Å in Z-direction to address the image of charge transfer and eliminate interaction between the neighbouring layers. For non-self-consistent calculations, a much denser MP grid of 12 x 12 x 1 is considered for finer accuracy in the results. For calculating electronic band structure, Γ-X-Y-Γ high symmetry path is considered. An external electric field is applied in ±Z-direction to realize the electric field effect in band topology (shown in appendix figure A3). To perform the charge transport property, BoltzTrap2 code [38] is employed with 16 x 16 x 1 dense K-point grid. Fermi surface (FS) is exported from Fermi surfer tool [39].

6.3 Result and Discussions

6.3.1 Geometry optimization

Figure 6.1 (a-c) represents the atomic configuration and ground state optimization of 1T'WTe_2-$CrBr_3$ van der Waals heterostructure. The optimized geometry and interplanar spacing of corresponding vdW heterostructure is obtained by employing Feynman-Hellman theorem. The interplanar distance d between the adjacent layers is 3.68 Å. The bilayer achieves ground state energy by considering ferromagnetic arrangement and vdW interaction. Here, we consider the monolayers of different lattice arrangement of atoms such as distorted octahedral (1T'-WTe_2) and hexagonal $CrBr_3$ as shown in figure 6.1 (d, g), respectively. The crystal atomic configuration for isolated monolayers (MLs) are optimized with a lattice parameter of 10.99 Å and 3.49 Å for ML-$CrBr_3$ and ML-1T'WTe_2, respectively shown in figure 6.1 (e, h). For quantitative assessment, the thermodynamic stability of vdW heterostructure is determined by calculating the binding energy (E_{bin}) as per the concerned equation, $E_{bin} = E_{het}-[(E_{WTe2}+E_{CrBr3})]/N$, where, E_{het}, E_{WTe2}, E_{CrBr3} describes the total energies obtained self-consistently from *ab initio* calculations for heterostructure, pristine WTe_2, $CrBr_3$ monolayers and N describes the number of atoms in corresponding unit cell (N=34). The obtained total energies are E_{het} = -

4719.57061738 Ry, E_{WTe2} = -1273.44696972 Ry and E_{CrBr3} = -3446.02367442 Ry, respectively. The binding energy is obtained as -39.9 meV at an interplanar distance of 3.68 Å, which is favourable with binding energy of vdW systems [40]. The negative binding energy indicates the heterostructure to be thermodynamically stable. To design 1T′-WTe_2/$CrBr_3$ vdW heterostructure, the unit cell of monolayer $CrBr_3$ must match the unit cell of 1T′-WTe_2. In this regard, the lattice mismatch between the adjacent layers is 2.9%, making it favourable for experimental realization. The optimum value of lattice parameter *a* is found to be 20.7 Å for the heterostructure system as shown in figure 6.1 (b).

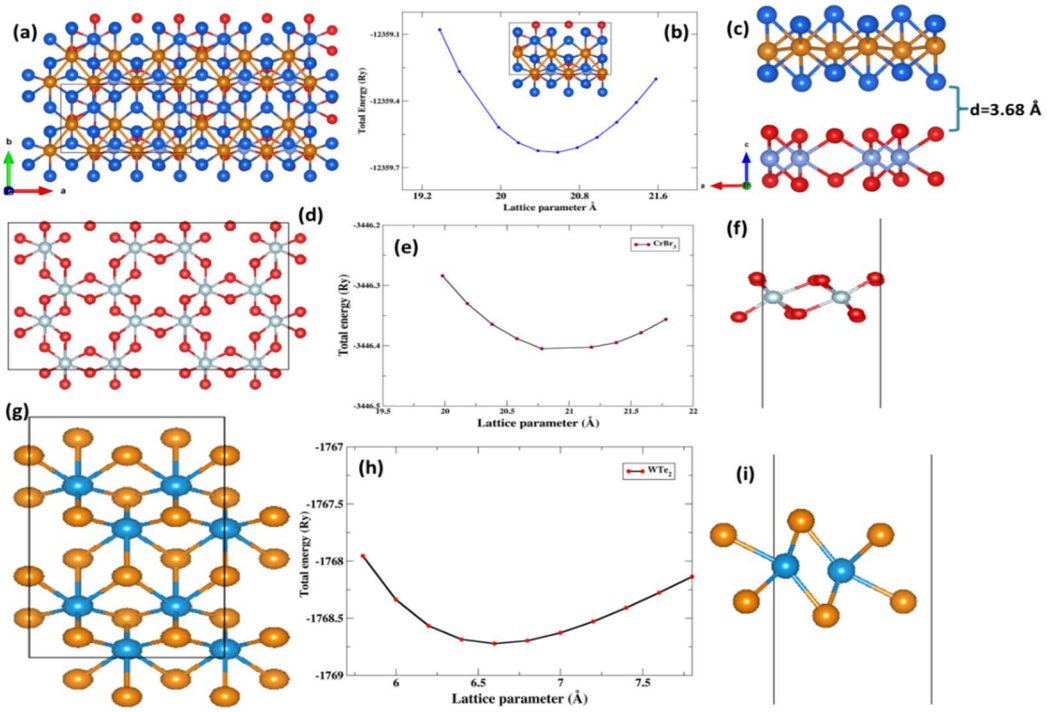

Figure 6.1: Atomic configuration of crystal structure. Top-view (a) 1T′-WTe_2/$CrBr_3$ supercell (d) $CrBr_3$, (g) 1T′-WTe_2. (c) Side view of the vdW heterostructure with interlayer distance d = 3.68 Å, (f) isolated $CrBr_3$, (i) monolayer 1T′-WTe_2. (b) Variation of Lattice parameter with total energy of the heterostructure system. Inset shows the unit cell of vdW heterostructure. The light blue, red, dark blue and orange spheres describe Cr, Br, W and Te atoms, respectively. Lattice parameter of (e) isolated $CrBr_3$, (h) individual 1T′-WTe_2.

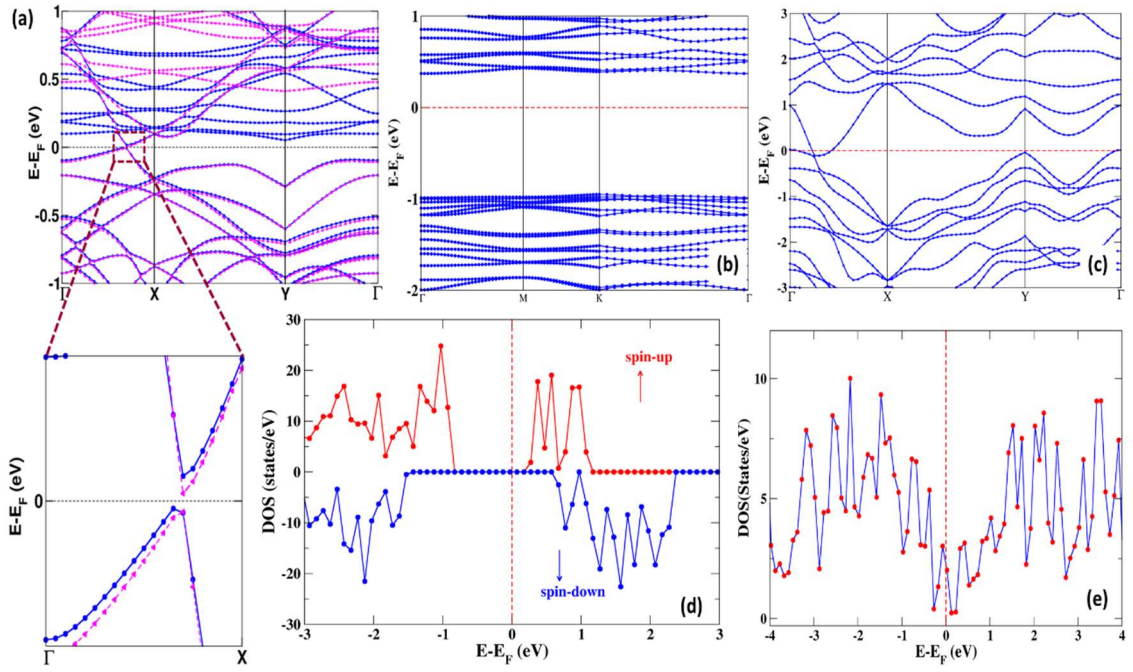

Figure 6.2: Electronic band structure of (a) vdW heterostructure without implications of relativistic effect. The blue continuous and magenta dotted lines depict spin up and down states, respectively. The zoomed-in image shows the spin-splitting in Γ-X high-symmetry points. (b, d) Band topology and density of states (DOS) of monolayer $CrBr_3$, (c, e) Band topology and density of states (DOS) of monolayer $CrBr_3$ 1T′-WTe_2

Figure 6.2 (a) corresponds to the electronic band structure of 1T′-WTe_2/$CrBr_3$ vdW heterostructure without relativistic effect at zero bias. It is known that monolayer $CrBr_3$ is a ferromagnetic semiconductor, while pristine 1T′-WTe_2 is a Weyl semimetal consisting of buckled layer of Te atoms and W atoms occupy in distorted octahedral sites [43]. For ML $CrBr_3$, distinct semiconducting nature is observed confirmed from figure 6.2 (b, d). Similarly, ML 1T′-WTe2 ascribes distinct semimetallic behaviour due to Weyl fermions along Γ-X symmetry points shown in figure 6.2 (c, e). In spin-polarized case, the presence of minimal energy band gap at Fermi level is observed within Γ-X high symmetry region. In magnified image of figure 6.2 (a), the minimal energy gap in 1T′-WTe_2 for spin-up and down states correspond to 0.025 eV (25 meV) and 0.013 eV (13 meV), respectively and the continuous energy gap along X-Y-Γ direction

depicts the character of $CrBr_3$. The minimal energy gap for 1T'-WTe_2 in heterostructure seems to be spin-splitted suggesting the presence of strong proximity coupling. It is seen that the electronic structure clearly resembles the combined characteristic of both monolayers due to magnetic proximity interaction between the adjacent layers. It can be noted that a very small gap of 0.013 eV is observed in case of spin down state, which we can assume to be zero. Therefore, such characteristic band topology speculates the presence of half-metallic character in vdW heterostructure system. Moreover, the overall characteristic of band structure is quite similar to the non-SOC case in presence of relativistic effect at zero electric field with slight overlap of conduction band minimum (CBM) at Fermi energy region. Despite the implication of SOC, the characteristic electronic band structure has no substantial changes due to which spin-polarized non-relativistic (non-SOC) effect has been considered only.

6.3.2 Electronic structure

The projected density of states ascribes the contribution of individual atomic orbitals for 1T'-WTe_2/$CrBr_3$ heterostructure. Figure 6.3 describes the spin-polarized PDOS pattern of the heterostructure system. It is seen from figure 6.3 (a), Br-p_y, p_z orbitals contribution is maximum for both spin-up and down configurations in the conduction band region. It is also evident that no characteristic peak for s-orbital is observed in both spin configurations. Figure 6.3 (b) displays the atomic orbital contribution of chromium atom present in the heterostructure system. It illustrates that conduction band region is mainly dominated by Cr-$4d_z$ orbitals for both spin configurations. In figure 6.3 (c), it is seen that the Te-p_y, p_z orbital is strongly hybridized in conduction band region with feebly hybridized s-orbital in both spin-up and spin-down configurations. Figure 6.3 (d) shows the major contribution or W-3d orbitals for both spin-up and spin-down directions, respectively. The contribution of W-3d orbitals is associated with the intense peak in the conduction band region. In this regard, it is clearly evident that Br, Te-p orbitals and Cr, W-d orbitals are actively

involved in hybridization of 1T′-WTe_2/$CrBr_3$ vdW heterostructure; the p- and d-orbitals are modified when they are brought in proximate distance. The total contribution of all the atomic orbitals is shown in Figure 6.3 (h). It is noticeable that p- and d-orbitals is actively influencing the hybridization in the heterostructure, which also corroborates well with figure 6.3 (a-d).

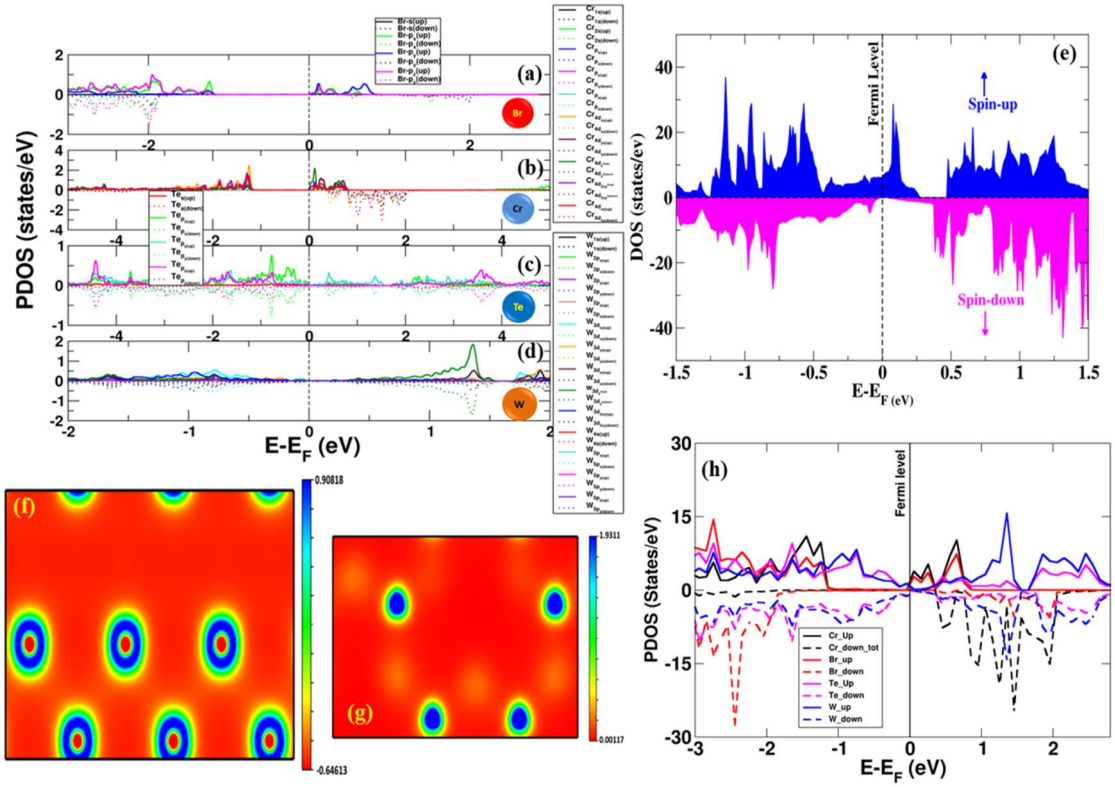

Figure 6.3: Electronic structure of 1T′-WTe_2/$CrBr_3$ vdW heterolayer. The calculated spin-polarized projected density of states (PDOS) for individual orbitals of vdW heterostructure: (a) bromine displayed as red colored spheres, (b) chromium as light blue colored spheres, (c) tellurium as blue colored spheres and (d) tungsten as orange-coloured spheres. (e) Spin-polarized total density of states (DOS) pattern of heterostructure system. The filled blue and magenta colour depicts spin-up and down configuration, respectively. (f) Charge density plot of (001) plane for bilayer system displays the top layer of 1T′-WTe_2 and (g) $CrBr_3$ layer. The positive and negative value in colour bar displays the electron localization and delocalization, respectively. (h) The total spin-polarized PDOS of vdW heterostructure system.

Figure 6.3 (e) depicts the spin-polarized density of states (DOS) for 1T'-$WTe_2/CrBr_3$ vdW heterostructure system. We observe that the spin up (blue continuous line) and down (magenta continuous line) states are asymmetric to each other in valence and conduction band region. Along with the asymmetric behaviour, the sharp peaks suggest the presence of magnetic character in the heterostructure system due to proximity effect. It is noticed that at Fermi level the spin up states are comparatively higher than that of spin down states which is nearly zero in the DOS pattern. In this regard, we calculate the spin-polarization (P) at Fermi level by considering the values of majority and minority spins, respectively. The spin-polarization percentage is found to be 100%, which infers that the system with semimetal-semiconductor characteristic transforms to half-metallic type behaviour. Therefore, the robustness of proximity effect substantially depends on orbital hybridization at interface of the system. Figure 6.3 (f and g) displays the charge density plot of (001) plane for 1T'-$WTe_2/CrBr_3$ heterostructure. Figure 6.3 (f) shows the charge density plot of WTe_2 layer of the heterostructure system. It is seen that the redistribution of charge occurs on the surface of tungsten atoms of the heterostructure system. The blue and yellow colour depicts the electron localization and delocalization near the central region of tungsten atoms. Figure 6.3 (g) represent the charge density mapping of $CrBr_3$ layer of heterostructure system, where blue and yellow colour depicts the electron accumulation and depletion. It is obvious that the blue region is more intense in the core region of Cr atoms because of its inherent magnetic character. Therefore, it is clearly evident that the reorganization of charge on the surface of vdW heterostructure system. We also calculate the magnetic anisotropy energy (MAE) with respect to magnetization angle, with 0° in plane and 90° out of plane, respectively. The value obtained by self-consistent calculation for heterostructure system is found to be around 6 meV, which is much higher than the pristine Cr-trihalides system [41, 42]. The ferromagnetic ordering was found in the ground state while conducting the spin polarized self-consistency calculation of the heterostructure gives total

magnetization value to be 12.04μ_B/cell. The magnetic moment value in heterostructure increases with an enhancement of 4% in contrast to the bulk $CrBr_3$ value ensures the implementation of magnetic proximity effect. Interestingly, the magnetism is induced in individual nonmagnetic layer of 1T′-WTe_2 in the heterostructure system. The averaged magnetic moment for W atom is -0.0022μ_B and -0.0018μ_B for Te atom. The magnetic moment further increases with an increment of ±0.04μ_B/cell as shown in figure 6.4 with the incorporation of external electric field in the range of ±0.5 V/Å (appendix figure A3) advocates the magnetic proximity effect to be highly sensitive towards external biasing making it favorable for developing spintronic devices.

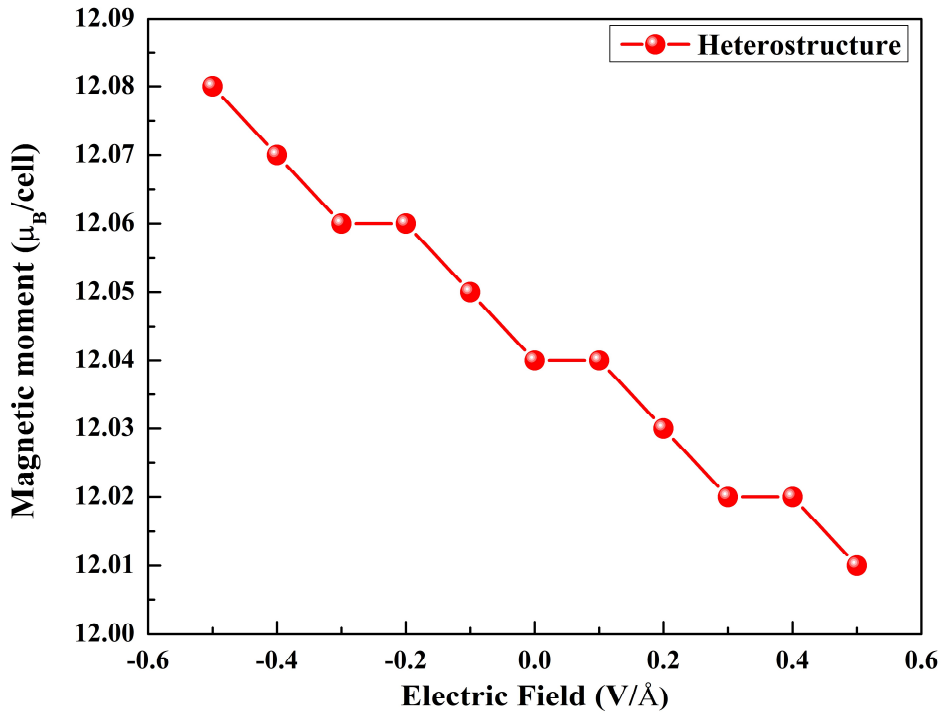

Figure 6.4: The variation of magnetic moment value for 1T′-WTe_2/$CrBr_3$ heterostructure as a function of applied electric field in 0 to ±0.5 V/Å.

6.3.3 Modulation of electronic structure with applied electric field

Figure 6.5 (a) represents the modulation of band gap as a function of external electric field in the window of 0 to ±0.5 V/Å. It is seen from figure 6.5 (a), that the appropriate non-linearity is observed under biasing, corresponding to

interlayer polarization effect. Moreover, the band gap overlapped at reverse biasing (-0.5 V/Å), while the band gap is widened at forward biasing (0.5 V/Å) for both spin configurations (appendix figure A3). The attraction and repulsion signify that the external stimulus disintegrate the equilibrium condition between diffusion and drift force exhibit from built-in electric field leading to interfacial polarization across the interface of adjacent layers. At forward bias, the external electric field in positive direction adds to built-in field leading to semiconducting nature keeping the spin-split unaltered. Meanwhile, at reverse bias, the external electric field is intense enough to remunerate the built-in field leading to overlapping states and bands are nearly at similar potential. Such characteristic band topology in presence of external bias gives rise to switching ability in heterostructure system. The spin-splitting between two spin configurations is clearly seen at zero bias. In case of reverse biasing, the charge transfer increases from WTe_2 to $CrBr_3$ layer leading to band offset between the adjacent monolayers. In contrast, the direction of forward biasing is opposite to in-built electric field due to which intrinsic field weakens and the charge transfer from WTe_2 to $CrBr_3$ reduces. This nature suggests the reduction in band offset between the adjacent layers. The half-metallicity is clearly observed from electronic structure due to the existence of proximity interaction, while proximity effect together with external stimulus transform the half-metallicity to semiconducting and overlapping nature in heterostructure system. It is evident that the external electric field can possibly tune the proximity interaction in heterostructure system. The non-linear nature of energy band gap and magnetic moment value suggests high degree of tunability with applied electric field in heterostructure system, which encourages the charge conductivity exclusively from one spin direction and interfacial polarization in heterostructure system. Figure 6.5 (b) represents the modulation of Fermi level with respect to external electric field in both ±Z-directions. The Fermi energy region situates at the surface of an energy level known as charge neutrality level, beneath which energy levels are occupied. It is observed that non-

uniformity exists in both forward and reverse bias, signifying the non-uniformity component. In reverse (forward) bias, the Fermi level shifts and energy bands overlaps (widens) along with the increase (decrease) in density of states at Fermi level. The modulation of Fermi level tunes electron and hole densities at the interface of the heterostructure system. As a consequence, the edge polarization becomes active at the surface states leading to collective behaviour of interlayer polarization.

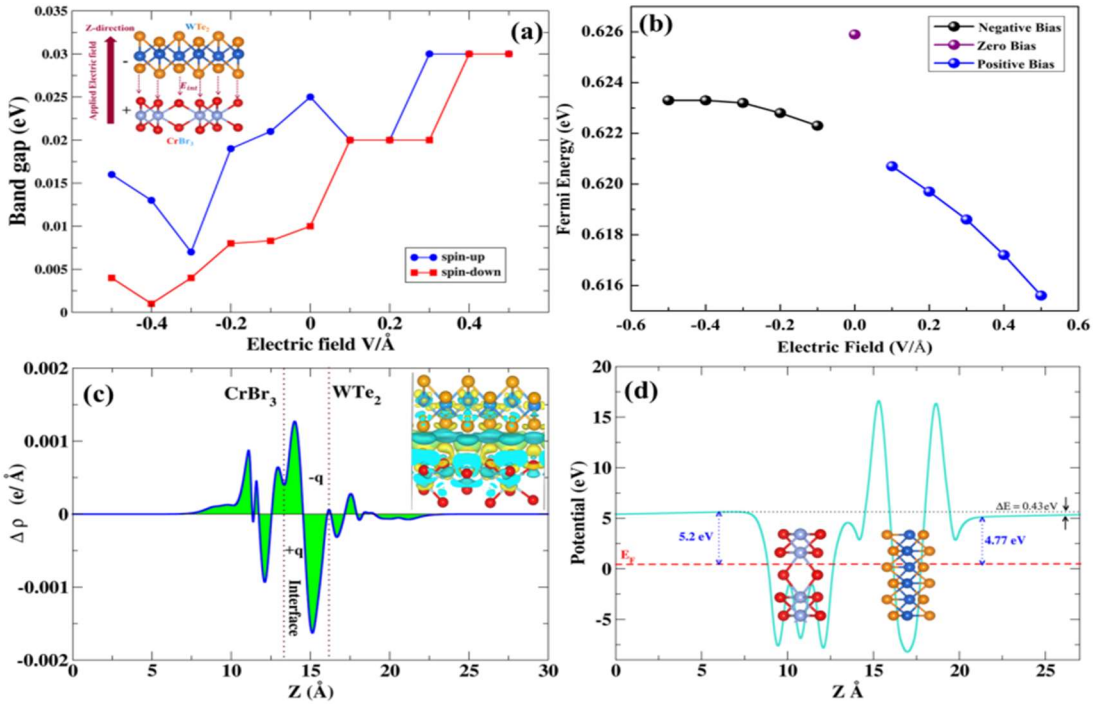

Figure 6.5: (a) The modulation of energy band gap as a function of external electric field in vdW heterostructure (inset shows the built-in electric field at interface leading to interfacial polarization under external electric field). (b) Variation of Fermi energy with respect to external electric field from -0.5 to 0.5 V/Å. (c) Plane averaged charge density difference Δρ, perpendicular to the interface along Z-direction (inset shows the 3D differential charge density with the isosurface value of 0.0001733 e/Å^3 for the heterostructure system. (The Yellow and cyan colour represents electron accumulation and depletion, respectively.) (d) The electrostatic potential of 1T'-WTe_2/$CrBr_3$ heterostructure along Z-direction.

In order to realize the underlying mechanism of charge transfer, we represent plane-averaged charge density and differential charge density shown in figure 6.5 (c). The plane-averaged charge density difference ($\Delta\rho$) is characterized as $\Delta\rho = \rho_{het}-\rho_{WTe2}-\rho_{CrBr3}$ and plotted against Z-direction to realize the redistribution of charge at the interface. It is clearly evident from the inset of figure 6.5 (c), the charge density is redistributed at the interface by electron depletion (cyan) around WTe_2 layer and electron accumulation (yellow) close to $CrBr_3$ layer in the heterostructure system. The negative and positive value marks charge depletion and accumulation region, respectively. The charge reorganization suggests that the charge transfer will occur from WTe_2 layer to $CrBr_3$ layer across the interface. The occurrence of charge transfer signifies the presence of intrinsic dipole (ΔE=0.45 eV) from 1T'-WTe_2 to $CrBr_3$ layer leading to inherent electric field and energy difference at the interface to modulate the Fermi level of vdW heterostructure system (shown in Figure 6.5 (d)). When WTe_2 exerts staggered potential on $CrBr_3$ layer, it stabilizes Fermi level and subject electrons from WTe_2 layer to $CrBr_3$ layer with the work functions value of 4.77 eV and 5.2 eV, respectively. These observations further confirm that the WTe_2 and $CrBr_3$ are ideally bonded to each other and enable substantial charge transfer from WTe_2 to $CrBr_3$ layer due to presence of proximity interaction. Hence, proximity effect plays an important role in charge transfer phenomena and motivates to realize the nature of electronic conductivity of the present heterostructure system.

6.3.4 Electrical conductivity

Figure 6.6 (a) displays the electronic conductivity of vdW heterostructure at zero electric field. To realize the charge transport phenomena at interface of heterostructure, the conductivity calculations are executed using BoltzTrap2 code under constant relaxation time approximation (CRTA) approach. It is clearly evident that the highly intense peak is observed in positive chemical potential region, where the electrons act as majority charge carriers (i.e., n-type)

and holes act as minority charge carrier (i.e., p-type) with less intense peak in negative chemical potential region. This correlates well with occurrence of electron accumulation and depletion explained by differential charge density shown in the inset of figure 6.5 (c), which confirms the presence of robust proximity interaction. Moreover, the conductivity value is found to be of the order of 10^6 Sm^{-1} at room temperature. From the overall spectra of conductivity, it is observed that both majority and minority carriers participate to obtain high electrical conductivity in heterostructure system. Figure 6.6 (b) facilitates the Fermi surface (FS) of 1T'-WTe_2/$CrBr_3$ vdW heterostructure system. The FS plot displays the surface in momentum space which describes the electronic state at stable energy. The blue region in Brillouin zone of Fermi surface depicts low concentration of electrons and red semi-circle at the edge of Brillouin zone signifies high electron concentration. The zone with high electron concentration (red) represents the characteristic of $CrBr_3$ and with low electron concentration (blue) zone describes the characteristic of 1T'-WTe_2 layer. The electron concentrations represented in FS plot can also be correlated from charge density difference, where the electrons accumulate in $CrBr_3$ layer and deplete from WTe_2 layer making it favorable for charge conduction. It is clearly evident that the energy contours depicted from Fermi surface facilitates the character of both 1T'-WTe_2 and $CrBr_3$ layer in Brillouin zone due to presence of active proximity coupling in the heterostructure system.

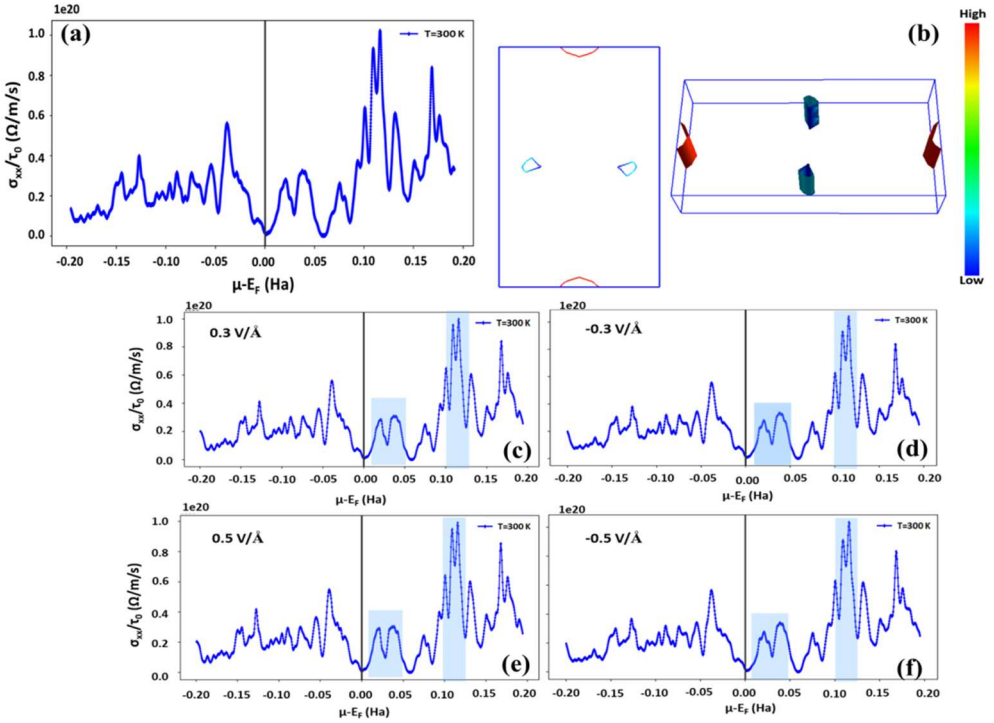

Figure 6.6: (a) Electronic conductivity of 1T′-WTe_2/$CrBr_3$ vdW heterostructure without external electric field. (b) Fermi surface (FS) of the heterostructure system. The colour bar describes the high (red) and low (blue) electron concentration, respectively. (c-f) Electronic conductivity of heterostructure system in presence of external stimuli for both forward and reverse biasing, respectively.

Figure 6.6 (c-f) represents the electronic conductivity in presence of external electric field in both forward and reverse directions, respectively. The chemical potential (μ) window between 0.00-0.05 Ha and 0.10 Ha are found to be shifted and intensity of the peak modulates in inclusion of external electric field in forward and reverse directions. In reverse bias at μ=0.10 Ha, the intensity of highest peak slightly decreases as compared to forward and no bias (figure 6.6 (a)). The same is observed for μ between 0.00-0.05 Ha. Moreover, the order of 10^6 S/m persists even after applying external electric field, which suggests the charge transport phenomena is controlled and making it promising for DG-FET applications. It is seen that with application of external electric field the conductivity profile slightly modulates and the nature remains substantially

unaffected. Therefore, external electric field is necessary to modulate the flow of electrons from source to drain by confining the transport channel and presence of electrostatic potential at interface of heterostructure system. The congruous behaviour of conductance profile suggests the control of in-built electric field (polarization) and efficient flow of electrons throughout the transport channel because of seamless proximity integration for its feasibility in developing DG-FET devices as described in figure 6.7 (b).

6.3.5 Proposed device prototype

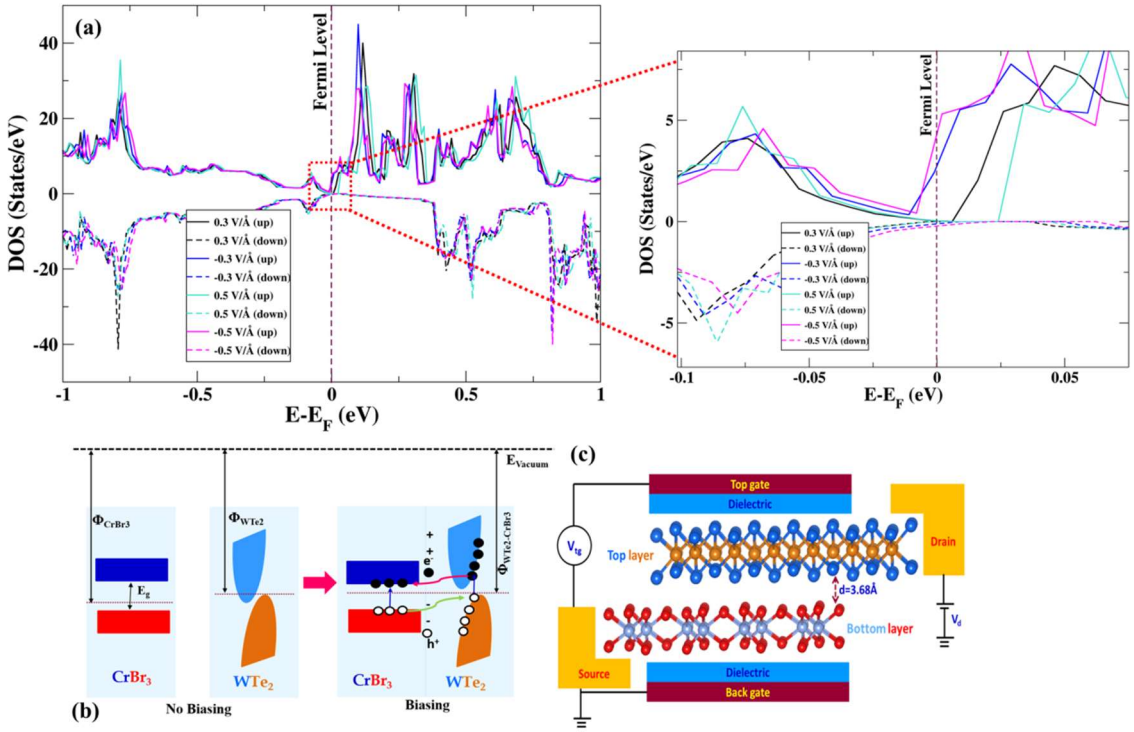

Figure 6.7: (a) Spin-polarized density of states (DOS) as a function of external electric field in both forward and reverse bias of the heterostructure system. Magnified image of spin-polarized DOS at Fermi level with external biasing. (b) Energy band diagram of 1T′-WTe_2/$CrBr_3$ vdW heterostructure without and with biasing. (c) Schematic representation of proposed device prototype for dual gate field effect transistor (DG-FET).

Figure 6.6 (a) displays the electric field mediated DOS as a function of Fermi energy in 1T′-WTe_2/$CrBr_3$ vdW heterostructure system for two spin

configurations. It is quite evident that near Fermi level in reverse biasing the overlapping state is visible for both spin configurations. In forward biasing, the gapped states are clearly observed for spin up and down states, respectively. It is also clearly seen from the magnified image of figure 6.5 (a). Figure 6.6 (a) also corroborates well with figure 6.2 (a). It is also evident from figure 6.6 (a), with reverse biasing the valence band crosses the Fermi level with overlapping states but it still persists the half-metallic nature making it suitable for spin filtering applications.

The energy band diagram of 1T'-WTe_2/$CrBr_3$ heterostructure is schematically shown in figure 6.6 (b). The semimetallic WTe_2 on the top of $CrBr_3$ layer exerts staggered potential at the interface with a finite distance of d=3.68 Å to realize the charge transfer and charge distribution modified in the heterostructure system. An external stimulus (electric field) is applied perpendicularly in both forward and reverse directions along Z-axis followed by ferromagnetic state. The energy band diagram is also influenced by the electrostatic potential of pristine monolayers (shown in appendix A4 (a) and (b)) and heterostructure shown in figure 6.5 (d). The monolayer $CrBr_3$ exhibits larger work function Φ (5.19 eV) than that of 1T'-WTe_2 pristine system (4.47 eV) shown in appendix A4 (a) and (b). In this regard, the charge transfer will occur between 1T'-WTe_2 layer and $CrBr_3$ layer followed by intrinsically built electric field leading to efficient recombination of electrons and holes. In presence of biasing, the charge transfer becomes extensive and increases the recombination lifetime of electrons and holes. In heterostructure system, the work function is found to be 4.77 eV higher than that of monolayer 1T'-WTe_2 and smaller than that of $CrBr_3$ layer (5.2 eV), which realigns the Fermi energy region. The device prototype of dual gate field-effect transistor (DG-FET) is displayed in figure 6.7 (c). The device comprises of source, drain, transmission channel and two gates for inclusion of external electric field. The vdW heterostructure is sandwiched between top gate, dielectric and back gate connected with source and drain in the centre region. The top gate and back gate are placed above and below the centre

region for applying external stimuli in proximitized heterostructure system. Because of proximity interaction, at zero biasing the heterostructure shows half-metallic behaviour that can be utilized as spin-filtering device. Moreover, application of external bias efficiently modulates the energy gap and transition occurs from half-metallic to semiconducting and overlapping states making it promising candidate for tunnel FET applications.

6.4 Concluding remarks

In conclusion, we demonstrate the presence of magnetic proximity interaction in 1T'-WTe_2/$CrBr_3$ vdW heterostructure system on the basis of first-principles simulation. The electronic structure reveals that the heterostructure exhibit half-metallic type nature, where spin polarization is induced in 1T'-WTe_2 with a spin-polarization of 100% originating by proximity coupling with ferromagnetic $CrBr_3$. A spin-splitting (small energy gap) of 25 meV and 10 meV for both spin configurations is observed, with a total magnetization of 12.04 μ_B per cell in the heterostructure system, 4% higher than that of pristine $CrBr_3$ layer. The electronic structure, charge transfer and spin splitting at interface strongly rely on 1T'-WTe_2/$CrBr_3$ vdW heterostructure at interlayer distance of 3.68 Å, which can be effectively tuned by external electric field. The charge transfer and electrostatic potential reinforces the in-built electric field, which triggers the screening from WTe_2 to $CrBr_3$ due to proximity coupling and suggests conductivity in the heterostructure system. The heterostructure system is found to be consistent with a slight shift in peaks and displays electronic conductivity to be of the order of 10^6 S/m, which remains unchanged even with inclusion of electric field. The magnetic proximity effect in the vdW heterostructure system has high degree of tunability in presence of electric field, the magnetic moment increases from 12.04 μ_B per cell to 12.08 μ_B per cell. Our findings suggest that magnetic proximity effect along with electric field will provide efficient spin injection phenomena in developing electric field mediated spin-filter as well as dual gate field effect transistor (DG-FET) applications.

References

[1] Gong, C., Li, L., Li, Z., Ji, H., Stern, A., Xia, Y., Cao, T., Bao, W., Wang, C., Wang, Y., Qiu, Z.Q., Cava, R.J., Louie, S.G., Xia, J. and Zhang, X. Discovery of intrinsic ferromagnetism in two-dimensional van der Waals crystals. *Nature,* 546:265–269, 2017.

[2] Novoselov, K. S., Mishchenko, A., Carvalho, A. and Castro Neto, A. H. 2D Materials and van der Waals Heterostructures. *Science*, 353:aac9439, 2016.

[3] Bonilla, M., Kolekar, S., Ma, Y., Diaz, H.C., Kalappattil, V., Das, R., Eggers, T., Gutierrez, H. R., Phan, M. -H. and Batzill, M. Strong room-temperature ferromagnetism in VSe_2 monolayers on van der Waals substrates. *Nature Nanotechnolorgy*, 13:289–293, 2018.

[4] Zhuang, H L. and Hennig, R G. Stability and magnetism of strongly correlated single-layer VS_2. *Physical Review B,* 93:054429, 2016.

[5] Bora, M. and Deb, P. Magnetic proximity effect in two-dimensional van der Waals heterostructure. *Journal of Physics: Materials*, 4:034014, 2021.

[6] Zhong, D., Seyler, K. L., Linpeng, X., McGuire, M. A., Fu, K -M. C., Xiao, D., Yao, W. and Xu, X. Layer-resolved magnetic proximity effect in van der Waals heterostructures. *Nature Nanotechnology,* 15:187, **2020**.

[7] Choi, E-M., Sim, K. I., Burch, K. S. and Lee, Y. H. Emergent multifunctional magnetic proximity in van der Waals layered heterostructures. *Advanced Sciences,* 9:2200186, 2022.

[8] Lazic, P., Belashchenko, K. D. and Zutic, I. Effective gating and tunable magnetic proximity effects in two-dimensional heterostructures. *Physical Review B,* 90:085429, 2016.

[9] Selver, S. and Majlis, N. Proximity effects in magnetic interfaces. *Physical Review B,* 33:4887, 1986.

[10] Yin, Z-B., Chen, X-Y., Wang, Y-P. and Long, M-Q. The magnetic proximity effect at the MoS_2/CrI_3 interface. *Journal of Physics: Condensed Matter,* 34:035002, 2021.

[11] Behera, S K., Bora, M., Chowdhury, S. S. P. and Deb, P. Proximity effects in graphene and ferromagnetic $CrBr_3$ van der Waals heterostructure. *Physical Chemistry Chemical Physics*, 21:25788, 2019.

[12] Bora, M., Behera, S. K., Samal, P. and Deb, P. Magnetic proximity induced valley-contrasting quantum anomalous Hall effect in a graphene-$CrBr_3$ van der Waals heterostructure. *Physical Review B,* 105:235422, 2022.

[13] Seyler, K. L., Zhong, D., Huang, B., Linpeng, X., Wilson, N. P., Taniguchi, T., Watanabe, K., Yao, W., Xiao, D., Mcguire, M. A., Fu, K-M. C. and Xu, X. Valley manipulation by optically tuning the magnetic proximity effect in WSe_2/CrI_3 heterostructures. *Nano Letters*, 18:3823, 2018.

[14] Wu, Y., Zhang, S., Zhang, J., Wang, W., Zhu, Y. L., Hu, J., Yin, G., Wong, K., Fang, C., Wan, C., Han, X., Shao, Q., Taniguchi, T., Watanabe, K., Zang, J., Mao, Z., Zhang, X. and Wang, K. L. Neel-type skyrmions in WTe_2/Fe_3GeTe_2 van der Waals heterostructure. *Nature Communications*, 11:3860, 2020.

[15] Talukdar, M., Behera, S. K., Jana, S., Samal, P. and Deb, P. Band alignment at heterointerface with rapid charge transfer supporting excellent photocatalytic degradation of methylene blue under sunlight. *Advanced Material Interfaces,* 9:2101943, 2022.

[16] Wimmer, S., Seemann, M., Chadova, K., Kodderitzsch, D. and Ebert, H. Spin-orbit induced longitudinal spin-polarized currents in nonmagnetic solids. *Physical Review B,* 92:041101, 2015**.**

[17] Lazic, P., Sipahi, G. M., Kawakami, R. K. and Zutic, I. Graphene spintronics: spin injection and proximity effects from first principles. *Physical Review B,* 90:085429, 2014.

[18] Liu, C., Wang, Z., Xiong, W., Zhong, H. and Yuan, S. Effect of vertical strain and in-plane biaxial strain on type-II $MoSi_2N_4/Cs_3Bi_2I_9$ van der Waals heterostructure. *Journal of Applied Physics,* 131:163102, 2022.

[19] Fulop, B., Marffy, A., Tovari, E., Kedves, M., Zihlmann, S., Indolese, D., Kovacs-Krausz, Z., Watanabe, K., Taniguchi, T., Schonenberger, C., Kezsmarki, I., Makk, P. and Csonka, S. New method of transport measurements on van der Waals heterostructures under pressure. *Journal of Applied Physics,* 130:064303, 2021.

[20] Xu, R. and Zou, X. Electric Field-Modulated Magnetic Phase Transition in van der Waals CrI_3 Bilayers. *Journal of Physical Chemistry Letters,* 11:3152, 2020.

[21] Zollner, K. and Fabian, J. Engineering proximity exchange by twisting: Reversal of ferromagnetic and emergence of antiferromagnetic Dirac bands in Graphene/$Cr_2Ge_2Te_6$. *Physical Review Letters,* 128:106401, 2022.

[22] Eremeev, S. V., Ottokov, M. M. and Chulkov, E. V. New Universal Type of Interface in the Magnetic Insulator/Topological Insulator Heterostructures. *Nano Letters,* 18:6521, 2018.

[23] Mohanty, S. and Deb, P. Nontrivial band topology coupled thermoelectrics in $VSe_2/MoSe_2$ van der Waals magnetic Weyl semimetal. *Journal of Physics: Condensed Matter,* 34:335801, 2022.

[24] Behera, S. K. and Deb, P. Controlling the bandgap in graphene/h-BN heterostructures to realize electron mobility for high performing FETs. *RSC Advances,* 7:31393, 2017.

[25] Piquemal-Banci, M., Galceran, R., Dubois, S. M. -M., Zatko, V., Galbiati, M., Godel, F., Martin, M-B., Weatherup, R. S., Petroff, F., Fert, A., Charlier, J-C., Robertson, J., Hofmann, S., Dlubak, B. and Seneor, P. Spin filtering by proximity effects at hybridized interfaces in spin-valves with 2D graphene barriers. *Nature Communications,* 11:5670, 2020.

[26] Song, K., Soriano, D., Cummings, A. W., Roberto, R., Ordejon, P. and Roche, S. Spin proximity effects in graphene/topological insulator heterostructures. *Nano Letters,* 18:2033, 2018.

[27] Qian, X., Liu, J., Fu, L. and Li, J. Quantum spin Hall effect in two-dimensional transition metal dichalcogenides. *Science,* 346:1344, 2014.

[28] Tang, S., Zhang, C., Wong, D., Pedramrazi, Z., Tsai, H-Z., Jia, C., Moritz, B., Claassen, M., Ryu, H., Kahn, S., Jiang, J., Yan, H., Hashimoto, M., Lu, D., Moore, R. G., Hwang, C-C., Hwang, C., Hussain, Z., Chen, Y., Ugeda, M. M., Liu, Z., Xie, X., Devereaux, T. P., Crommie, M. F., Mo, S -K. and Shen, Z -X. Quantum spin Hall state in monolayer 1T′-WTe_2. *Nature Physics,* 13:683, 2017.

[29] Feng, B. et al. Spin texture in type-II Weyl semimetal WTe_2. *Physical Review B,* 94:195134, 2016.

[30] Das, P. K. et al. Layer-dependent quantum cooperation of electron and hole states in the anomalous semimetal WTe_2. *Nature Communications,* 7:10847, 2016.

[31] Johansson, A., Henk, J. and Mertig, I. Edelstein effect in Weyl semimetals. *Physical Review B,* 97:085417, 2018.

[32] Hasan, M. Z. and Kane, C. L. Colloquium: Topological insulators. *Review Modern Physics,* 82:3045, 2010.

[33] Ghazaryan, D., Greenaway, M. T., Wang, Z., Guarochico-Moreira, V. H., Vera-Marun, I. J., Yin, J., Liao, Y., Morozov, S. V., Kristanovski, O., Lichtenstein, A. I., Katsnelson, M. I., Withers, F., Mishchenko, A., Eaves, L., Geim, A. K., Novoselov, K. S. and Misra, A. Magnon-assisted tunnelling in van der Waals heterostructures based on $CrBr_3$. *Nature Electronics,* 1:344, 2018.

[34] Giannozzi, P., Baroni, S., Bonini, N., Calandra, M., Car, R., Cavazzoni, C., Ceresoli, D., Chiarotti, G. L., Cococcioni, M., Dabo, I., Corso, A. D., de Gironcoli, S., Fabris, S., Fratesi, G., Gebauer, R., Gerstmann, U., Gougoussis, C., Kokalj, A., Lazzeri, M., Martin-Samos, L., Marzari, N., Mauri, F., Mazzarello, R., Paolini, S.,

Pasquarello, A., Paulatto, L., Sbraccia, C., Scandolo, S., Sclauzero, G., Seitsonen, A. P., Smogunov, A., Umari, P., and Wentzcovitch, R. M. QUANTUM ESPRESSO: a modular and open-source software project for quantum simulations of materials. *Journal of Physics: Condensed Matter*, 21(39):395502, 2009.

[35] Perdew, J. P., Burke, K. and Ernzerhof, M. Generalized gradient approximation made simple. *Physical Review Letter*, 77:3865, 1996.

[36] Grimme, S. Semiempirical GGA-type density functional constructed with a long-range dispersion correction. *Journal of Computational Chemistry*, 27(15):1787–1799, 2006.

[37] Wu, Z., Liu, X., Shen, Z., Xue, Y., Wu, X., Zhong, T., Wang, J., Pan, J., Li, C. and Song, C. Band shifting and magnetic anisotropy switching induced by electric field in CrI_3/1T'-MX2 heterojunction. *Journal of Physics D: Applied Physics,* 54:395302, 2021.

[38] Madsen, G. K. H. and Singh, D. J. BoltzTrap. A code for calculating band-structure dependent quantities. *Computer Physics Communication*, 175:67, 2006.

[39] Kawamura, M. FermiSurfer: Fermi-surface viewer providing multiple representation schemes. *Computer Physics Communication,* 239:197, 2019.

[40] Hod, O. Graphite and Hexagonal Boron-nitride have the same interlayer distance. Why? *Journal of Chemical Theory and Computation,* 8:1360, 2012.

[41] Webster, L. and Yan, J-A. Strain-tunable magnetic anisotropy in monolayer $CrCl_3$, $CrBr_3$ and CrI_3. *Physical Review B,* 98:144411, 2018.

[42] Li, Z., Zhou, B. and Luan, C. Strain-tunable magnetic anisotropy in two-dimensional Dirac half-metals: Nickel trihalides. *RSC Advances,* 9:35614, 2019.

[43] Lee, C-H., Silva, E. C., Calderin, L., Nguyen, M. A. T., Hollander, M. J., Bersch, B., Mallouk, T. E. and Robinson, J. A. Tungsten Ditelluride: a layered semimetal. *Scientific Reports,* 5:10013, 2015.

[44] Michetti, P., Recher, P. and Iannaccone, G. Electric field control of spin rotation in Bilayer graphene. *Nano Letters,* 10:4463, 2010.

[45] Shayan, K., Liu, N., Cupo, A., Ma, Y., Luo, Y., Meunier, V. and Strauf, S. Magnetic proximity coupling of quantum emitters in WSe_2 to van der Waals ferromagnets. *Nano Letters,* 19:7301, 2019.

[46] Haifeng, L., Niu, Y., Wu, X. and Yang, J. Electric-Field Tunable Magnetism in van der Waals Bilayers with A-Type Antiferromagnetic Order: Unipolar versus Bipolar Magnetic Semiconductor. *Nano Letters,* 21:7050, 2021.